processes

MDPI

Article

Analysis of Flow Field and Machining Parameters in RUREMM for High-Precision Micro-Texture Fabrication on SS304 Surfaces

Wenjun Tong [1,2] and Lin Li [3,*]

[1] Department of Mechanical Engineering, Ningbo Polytechnic, 288, Lushan Road, Ningbo 315800, China; wenjuntong@126.com
[2] College of Mechanical Engineering, Southeast University, Nanjing, 210008, China
[3] College of Mechanical Engineering, Zhejiang University of Technology, Hangzhou, 310014, China
* Correspondence: linli@zjut.edu.cn

Abstract

Micro-textures are crucial for enhancing surface performance in diverse applications, but traditional radial electrochemical micromachining (REMM) suffers from process complexity and workpiece damage. This study presents radial ultrasonic rolling electrochemical micromachining (RUREMM), an advanced technique integrating an ultrasonic field to improve electrolyte renewal, disrupt passivation layers, and optimize electrochemical reaction uniformity on SS304 surfaces. Aimed at overcoming challenges in precision machining, the research explores the synergistic effects of ultrasonic energy and flow field dynamics, offering novel insights for high-quality metal micromachining applications. The research establishes a mathematical model to analyze the interaction between the ultrasonic energy field and electrolytic machining and optimizes the flow field in the narrow electrolytic gap using Fluent software, revealing that an initial electrolyte velocity of 4 m/s and ultrasonic amplitude of 35 μm ensure optimal stability. High-speed photography is employed to capture bubble distribution and micro-pit formation dynamics, while SS304 surface experiments analyze the effects of machining parameters on micro-dimple localization and surface quality. The results show that optimized parameters significantly improve micro-texture quality, yielding micro-pits with a width of 223.4 μm, depth of 28.9 μm, aspect ratio of 0.129, and Ra of 0.205 μm, providing theoretical insights for high-precision metal micromachining.

Keywords: radial electrochemical micromachining; ultrasonic field; bubble distribution; model optimization; micro-pit morphology

check for updates

Academic Editor: Keith J. Stine

Received: 10 June 2025
Revised: 7 July 2025
Accepted: 17 July 2025
Published: 22 July 2025

Citation: Tong, W.; Li, L. Analysis of Flow Field and Machining Parameters in RUREMM for High-Precision Micro-Texture Fabrication on SS304 Surfaces. *Processes* **2025**, *13*, 2326. https://doi.org/10.3390/pr13082326

Copyright: © 2025 by the authors. Licensee MDPI, Basel, Switzerland. This article is an open access article distributed under the terms and conditions of the Creative Commons Attribution (CC BY) license (https://creativecommons.org/licenses/by/4.0/).

1. Introduction

Nowadays, the fabrication of micro-textures with non-smooth morphologies and specific dimensional structures on the metal surface can significantly enhance the performance of products. Specifically, it can reduce friction and wear, decrease resistance, improve load-bearing capacity, and avoid surface adhesion and seizure, among other benefits [1–3]. Surface micro-textures can be applied in industrial fields such as aerospace, electronics, and automotive industries. For instance, they can be used in cooling air ducts and damping bushings of aerospace engines, as well as in gratings of electron microscopes and surface textures of pistons [4–6]. By applying micro-texturing treatment to mechanical seals, the contact temperature can be effectively reduced by 5–10%, thereby enhancing their working lifespan [7,8]. Compared with smooth surfaces, micro-textures can effectively

increase the surface area and the thermal diffusivity, thereby multiplying the heat transfer efficiency of the equipment [9,10]. During the machining process, the cutting tool is in continuous contact with the workpiece, enabling the processing of various complex shapes. However, due to the effect of stress, the workpiece undergoes deformation and tends to generate a large amount of heat, which affects the machining quality. The characteristic of non-traditional machining is that there is no contact between the workpiece and the tool. Instead, energy (electrical energy, optical energy, chemical energy) is highly concentrated on the workpiece surface to achieve the purpose of material removal, thus providing new possibilities for the processing of difficult-to-machine metals, complex surfaces, and micro-forming, such as laser beam machining (LSM) [11–14], micro-electrical discharge machining (EDM) [15–18], electrochemical micromachining (EMM) [19–23], and ion beam machining [24–26]. Compared with other methods, EMM boasts multiple advantages like high precision for micrometer-scale shaping, being non-thermal to avoid material damage, having good material compatibility, minimal tool wear, and remarkable three-dimensional machining ability for complex geometries [27–29]. Traditional EMM limitations: Previous works highlight challenges in flow field stability and passivation layer management, which limit machining precision.

The methodology of electrochemical micromachining has undergone significant evolution and changes. For example, electrochemical jet machining features a focused electrolyte jet for localized material removal, allowing high precision on various conductive materials, with the ability to create intricate patterns and maintain a relatively clean working environment during the process [30–33]. Electrochemical jet machining now uses a gas-assisted tool to enable deep-small hole machining for the first time [34], achieving localized material removal with precision suitable for ribbed surfaces of turbulated cooling holes, while traditional ECJM lacked such deep-hole capability. Liu et al. showed that the newly developed gas assistance tool enables the electrochemical jet machining process to be carried out in deep-small holes for the very first time, and the processing accuracy has been increased by 32.6%. Mask electrochemical micromachining (TMEMM) features precise patterning by using masks to control the electrochemical reactions, which allows for high-resolution fabrication of microstructures on conductive materials, with good reproducibility. Moreover, it can achieve complex geometries while maintaining relatively low costs and is suitable for batch production [35–37]. Yang et al. researched that two feeder electrodes function as the anode and cathode, respectively, giving rise to an electric field in which the wireless workpiece is positioned. A MEMS inertial switch was fabricated with high accuracy, achieving a non-uniformity of merely 3.8%. This represents a remarkable 96.2% enhancement in accuracy when compared to traditional TMEMM [38]. Electrochemical micro milling combines electrochemical dissolution with mechanical cutting. A tiny rotating tool electrode is used while electrolyte flows between it and the workpiece. It features high precision for microstructures, good surface finish, adjustable material removal rates, and can handle complex geometries effectively on conductive materials [39–41]. Shen et al. proposed that the several multichannel rotating cathodes with diverse designs of liquid outlet holes be put forward with the aim of enhancing the surface flatness in rotating-cathode electrochemical milling. Subsequently, a plane with dimensions of 42 × 40 mm is successfully machined, and its planeness index (Δhp) is merely 0.047, and the straightness index and depth error of the surface machined by the novel multichannel cathode are reduced by 80.9% and 69.4%, respectively [42]. Co-rotating electrochemical machining employs the co-rotation of electrodes and workpiece while applying an electrochemical process, with controlled electrical parameters and electrolyte flow, to precisely shape the workpiece by anodic dissolution for achieving desired geometries [43,44]. Zhou et al. fabricated an aero-engine casing whose inner surface features numerous irregular island structures. The fabricated

island structures have a height of 6 mm, and the sidewall thickness of the aero-engine casing is 1.2 mm through this method, and the average roughness of the machined surface is 0.494 μm, and the local maximum machining error of the top contours is 0.26 mm [45]. Air-shielding electrochemical micro-machining (AS-EMM) involves using air flow to protect the machining zone in the electrochemical process. By regulating electrolyte flow and electrical parameters precisely, it enables micro-material removal for creating high-precision microstructures with good quality [46,47]. Wang et al. found that verification experiments were conducted based on the comparison results of EMM and AS-EMM at different selected time steps, and the aggregated deviation between experimental and theoretical results was less than 11.8%. However, AS-EMM has several drawbacks; for instance, the stability of the air film is difficult to precisely control and is easily affected by processing parameters and external disturbances, thus influencing the machining accuracy, and the minimum island with a size of 130 × 130 μm and the surface roughness (Ra) of 154 nm could be obtained [48]. Additionally, the uneven distribution of the electrolyte flow field may lead to inconsistent machining surface quality, and the forming effect sometimes fails to meet the desired requirements when machining complex shapes.

In order to solve the above problems, researchers have conducted extensive explorations on diverse solutions in recent years. Of particular note is the application of ultrasonic field assistance, which has become increasingly popular in the energy field and has been integrated into relevant machining techniques. Owing to the cavitation and impact effects that the ultrasonic energy field can generate, it is capable of accelerating material removal and overcoming the anode passivation phenomenon, thereby enhancing the machining efficiency. Moreover, it can promote the renewal of the electrolyte, making the distributions of the electric field and flow field more uniform, which is conducive to improving the machining accuracy. It can also reduce the surface roughness of the machined parts and improve the surface quality [49–51]. Ren et al. carried out experiments under varying inlet pressure, vibration amplitude, and current density. The results showed that the electrolytic products on the machined surface could be removed through the ultrasonic vibration of the cathode tool, thereby leading to a smoother surface. A mirror surface with a surface roughness (Ra) of 0.14 μm was achieved with assisted ultrasonic energy. Compared with ultrasonic-assisted electrochemical machining (UA-EMM) reported by Ren [52], which achieved a surface roughness of 0.14 μm but suffered from unstable bubble accumulation at high amplitudes, RUREMM integrates radial ultrasonic vibration with sidewall-shielded flow fields to enhance electrolyte uniformity. Unlike the gas-assisted electrochemical jet machining by Liu et al. [34], which is limited to deep-small hole structures, our method enables precise micro-dimple arrays on flat SS304 surfaces with controlled aspect ratios. These improvements address the critical gap in balancing surface quality, feature localization, and process stability. Zhang et al. switched between the low-speed flow field and the high-speed flow field, thereby controlling the vertical and radial corrosion rates. Eventually, a microcone array with a height of 256.2 μm and a tip diameter of 20.3 μm was fabricated [53]. Chen et al. demonstrated that with the assistance of ultrasonic vibration and optimized parameters, a smooth microchannel with a width of 118.9 μm was fabricated, and its surface roughness was measured to be 0.23 μm, which represents an 80.99% decline from the 1.21 μm [54]. Wang et al. indicated that the machining depth diminished the effect of ultrasonic vibration. In comparison with EDM, ultrasonic-assisted EDM (UEDM) attained a 51.7% reduction in electrode wear, a 33.5% reduction in hole taper, and fewer microscopic defects [55]. Huang et al. researched that at a circumferential vibration frequency of 80 Hz, when the cathode feed rate is increased from 2.5 to 2.7 mm/min, a higher tooth profile (with a 5% improvement) and helical precision (with a 39.7% improvement), along with enhanced machining efficiency, can be obtained [56].

However, there still exist instances of stray corrosion in ultrasonically assisted electrochemical micromachining. While ultrasonic-assisted electrochemical micromachining has shown promise in enhancing material removal and surface quality, existing approaches still face challenges such as insufficient control over electrolyte flow uniformity, persistent issues with passivation layer accumulation, and residual stray corrosion due to uneven bubble distribution. Specifically, traditional REMM struggles with unstable flow fields in narrow gaps, leading to inconsistent current density, localized over-corrosion, and reduced machining precision. Although previous studies have explored ultrasonic integration, the synergistic effects of ultrasonic amplitude, electrolyte velocity, and gap geometry on flow field stability and micro-pit morphology remain underinvestigated. This research targets the critical gap of optimizing ultrasonic energy to regulate bubble dynamics, enhance electrolyte renewal, and mitigate passivation in REMM, thereby addressing the unresolved challenges of machining precision and surface integrity on SS304 surfaces. Studies demonstrated surface quality improvements via ultrasonic assistance but lacked systematic optimization of combined parameters. This summary contextualizes RUREMM as a solution to these unresolved issues, integrating radial ultrasonic vibration with sidewall-shielded flow fields for enhanced uniformity.

In this study, a novel micro-electrochemical machining technique—radial ultrasonic rolling electrochemical micromachining (RUREMM)—was proposed based on electrochemical machining technology and the principle of ultrasonic vibration. By utilizing the impact of micro-jets generated by ultrasonic vibration, it changes the flow state of the fluid field within the gap, promotes the renewal of the electrolyte in the machining area, and enhances the electric field distribution in the gap, thereby improving the surface quality, material removal rate, and roughness of micro-textures. First, a mathematical model was established to analyze the relationship between the ultrasonic energy field and electrolytic machining. The flow field in the narrow electrolytic machining gap was analyzed and optimized through Fluent, showing that the electrolyte flow velocity is more uniform with the sidewall-shielding method at 4 m/s and 35 μm amplitude for optimal stability. Second, high-speed photography was employed to study the RUREMM mechanism by capturing bubble distribution and analyzing micro-pit morphology formation over time. Micro-dimple arrays were created on SS304, considering machining parameters. Additionally, appropriate parameters can enhance micro-dimple localization and surface quality. Finally, pits with a width of 223.4 μm, depth of 28.9 μm, aspect ratio of 0.129, and Ra of 0.205 μm were formed, providing theoretical references for better metal surface processing. To propose a novel radial ultrasonic rolling electrochemical micromachining (RUREMM) technique integrating an ultrasonic field to enhance electrolyte renewal and electrochemical reaction uniformity on SS304 surfaces.

2. Principle of the RUREMM

Radial electrochemical micromachining (REMM) is a non-traditional machining technique that leverages anodic dissolution under an electric field to achieve precise material removal for micro-texture fabrication. In this process, a rotating cathode tool with radial symmetry is positioned relative to the workpiece anode, creating a narrow electrolytic gap where an electrolyte flows to facilitate electrochemical reactions. However, REMM encounters inherent limitations: The coordination of rotating cathode motion, electrolyte flow, and electrical parameters demands sophisticated system calibration. Combined forces from electrolytic reactions and mechanical rolling (during tool rotation) can induce surface defects or deformation, especially on ductile materials like SS304. Uneven electrolyte distribution in the narrow gap leads to inconsistent current density, causing localized over-corrosion and reduced machining precision. Figure 1 depicts the machining principle schematic of

RUREMM. The radial ultrasonic transducer (serving as the tool cathode), which features a microstructure of micro-bosses on its surface, is connected to the negative terminal of the power source and rotates around the spindle of the machine tool at a specific angular velocity. Meanwhile, the workpiece anode is linked to the positive terminal of the power source and undertakes translational motion in concert with the spindle of the machine tool, with the translational speed of the workpiece being identical to the linear velocity of the tool's rotation. During the machining process, the $NaNO_3$ electrolyte rushes out from the nozzle and impacts the machining gap. Under the influence of the ultrasonic transducer, the tool generates radial vibrations, which lead to the formation of a pulsating flow field within the machining gap. This, in turn, promotes the expulsion of electrolytic products and the renewal of the electrolyte. Under the effect of the electric field, an electrochemical reaction takes place between the two electrodes, and the principle of electrochemical anodic dissolution is harnessed to accomplish the objective of material removal. This technique integrates radial ultrasonic vibration into traditional electrochemical micromachining, leveraging ultrasonic-induced cavitation and micro-jet effects to enhance electrolyte renewal, disrupt passivation layers, and improve the uniformity of electrochemical reactions, thus enabling high-precision micro-texture fabrication on metal surfaces.

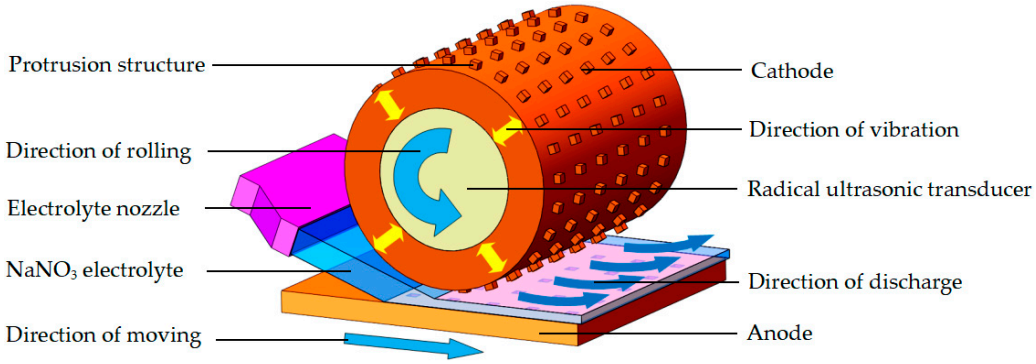


Figure 1. The schematic view of RUREMM.

During the RUREMM, the electrolyte continuously flows through the machining gap from leftward. The hydrogen ions near the exterior of the tool electrode acquire electrons and release H_2. Meanwhile, the dissolution of metal on the surface of the anode workpiece generates electrolytic products and simultaneously releases O_2, Cl_2, or CO_2. Consequently, numerous tiny bubbles of varying sizes and different distributions exist within the machining gap. When the generation rate of the bubbles exceeds the flow rate of the electrolyte, small bubbles continuously accumulate and coalesce to form larger bubbles, as shown in Figure 2a. The electrical conductivity of gas is far lower than that of the electrolyte. The presence and size of bubbles will alter the electric field distribution within the gap. Bubbles are continuously generated and diffused, and excessively large bubbles that are unevenly distributed will lead to uneven distribution of current density in the electrolytic region, thereby resulting in uneven material removal. This affects the diffusion of heat in the machining gap and the removal of corrosive impurities and ultimately influences the machining quality and machining efficiency.

When the ultrasonic energy field is applied, the bubbles within the machining gap will undergo cavitation phenomena, generating micro-jets with high frequency, high temperature, and high pressure. These micro-jets continuously scour the oxide layer on the workpiece surface and swiftly flush away the bubbles in the machining gap, preventing the small bubbles generated by electrolysis from accumulating on the surface of the tool electrode in a timely manner to form large bubbles, as depicted in Figure 2b. The flow field within the machining region changes, and the renewal rate of the electrolyte

accelerates. As a result, the small bubbles rapidly detach from the workpiece surface and accumulate into bubble clusters on the liquid surface. This timely removes the products of rolling electrochemical machining, takes away more heat, increases the current density and the material removal rate, and consequently enhances the efficiency of rolling-imprint electrochemical machining.

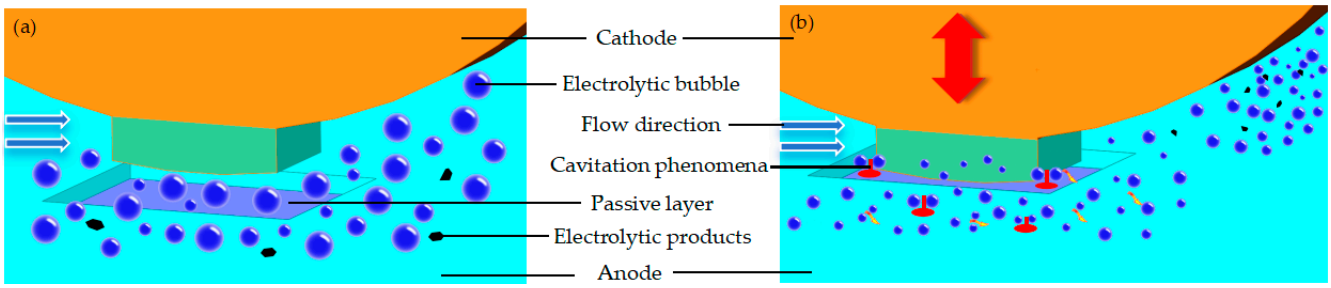


Figure 2. Schematic model of material anodic dissolution. (**a**) REMM; (**b**) RUREMM.

3. Theoretical Design

Motion Patterns of RUREMM Machining

During the machining process, the radial ultrasonic transducer rotates while simultaneously feeding forward along the surface of the workpiece. Ultrasonic vibrations generate vibration components (V_X, V_Z) in both the depth and width directions of the pit formation, as shown in Figure 3a. Under the action of these two components, its motion trajectory is similar to an elliptical vibration trajectory in Figure 3b, which improves the efficiency and precision of microstructure formation.

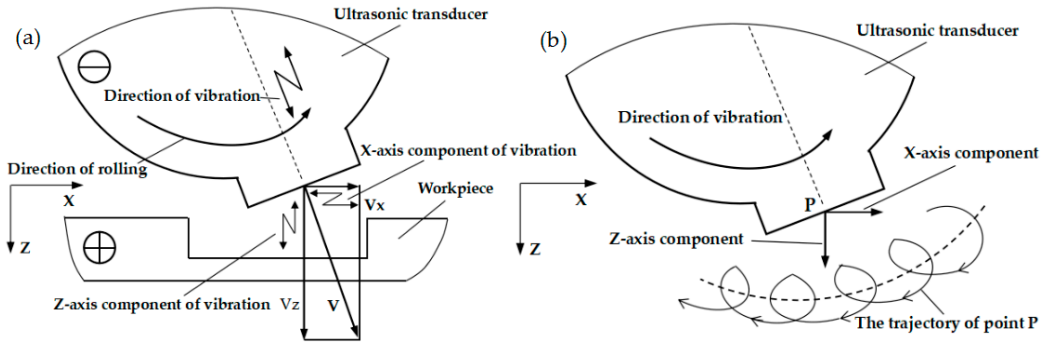


Figure 3. Schematic diagram of the motion in micro electrochemical machining excited by a radial ultrasonic energy field. (**a**) Motion schematic diagram; (**b**) Motion trajectory diagram.

Due to the existence of vibration in the Z direction, during the machining process, the relationship between the electrochemical machining gap between the anode of the workpiece and the cathode of the tool varies with time as follows [56]:

$$\Delta(t) = \Delta_Z + A\sin(2\pi f t) \quad (1)$$

where Δ_Z represents the initially set electrode gap, A is the amplitude of ultrasonic vibration, f is the frequency of ultrasonic vibration, and t is the machining time. Suppose that ξ is a point within the energization time region $[t_1, t_2]$, $t_k = t_2 - t_1$, $\eta\omega\sigma U_R$ are the electrical and liquid constants of electrochemical machining, $v(t)$ is the material removal speed

of the workpiece, and T is the period of ultrasonic vibration. Then, the depth of micro-electrochemical machining excited by the radial ultrasonic energy field is as follows [57]:

$$\int_{t_1}^{t_2} v(t)dt = \int_{t_1}^{t_2} \frac{\eta\omega\sigma U_R}{\Delta_Z + A\sin(2\pi ft)}dt = \eta\omega\sigma U_R \bullet \frac{t_k}{\Delta_Z + A\sin(2\pi ft \bullet \xi)} \quad (2)$$

Suppose that θ represents the angle between the cathode feeding direction and the normal of the workpiece profile. Then, based on the law of electrolytic dissolution, it can be derived as follows [57]:

$$\int_{t_1}^{t_2} v(t)dt = v \bullet T \bullet \cos\theta \quad (3)$$

According to Equations (2) and (3), the following equation is as follows:

$$v \bullet T \bullet \cos\theta = \eta\omega\sigma U_R \bullet \frac{t_k}{\Delta_Z + A\sin(2\pi f \bullet \xi)} \quad (4)$$

According to the correlation formulas, it can be derived from Equation (4), and the actual effective machining clearance is as follows [58]:

$$\Delta_Z = \frac{\eta\omega\sigma U_R}{v\cos\theta} \bullet \frac{t_k}{T} - A\sin(2\pi f \bullet \xi) \quad (5)$$

$$\Delta_E = \Delta_Z - A = \frac{\eta\omega\sigma U_R \bullet t_k}{v\cos\theta \bullet T} - A[1 + \sin(2\pi f \bullet \xi)] \quad (6)$$

As can be seen from Equation (6), the equivalent machining clearance is reduced compared with that in micro electrochemical machining. Ultrasonic vibration can improve the machining conditions in the micro-clearance machining area, avoid the short circuit between the cathode and the anode during small-clearance machining, and is highly conducive to improving the machining accuracy.

4. Simulation Design

In practical experimental setups, direct observation of the internal flow field details is highly challenging due to the extremely narrow machining gaps inherent in REMM. However, Ansys Fluent software 2024R1—by integrating relevant physical models and numerical algorithms—enables clear visual characterization of the flow field within these gaps. It intuitively depicts key flow field attributes, such as velocity distributions across distinct regions, thereby assisting researchers in accurately interpreting the flow dynamics.

4.1. Model Description

Figure 4 illustrates the schematic diagram of the dimensions of the FLUENT simulation model. The end part of the cathode tool electrode adopts a size of 400 × 400 μm. The spacing between electrodes is 800 μm. The radius of the rotary cathode tool is 50 mm, and the machining gap is 100 μm. The electrolyte flows in from the nozzle inlet on the right side and out from the sidewall outlet on the left side. The local refinement of grids in the Fluent simulation model can accurately capture the details in regions with drastic changes in the flow field. Meanwhile, on the premise of avoiding excessive denseness of the overall grids that would lead to a huge increase in computational load, it improves the computational accuracy of key local areas, facilitating in-depth analysis of local physical phenomena and optimizing the overall simulation effect. The dimensional parameters of the model are shown in Table 1.

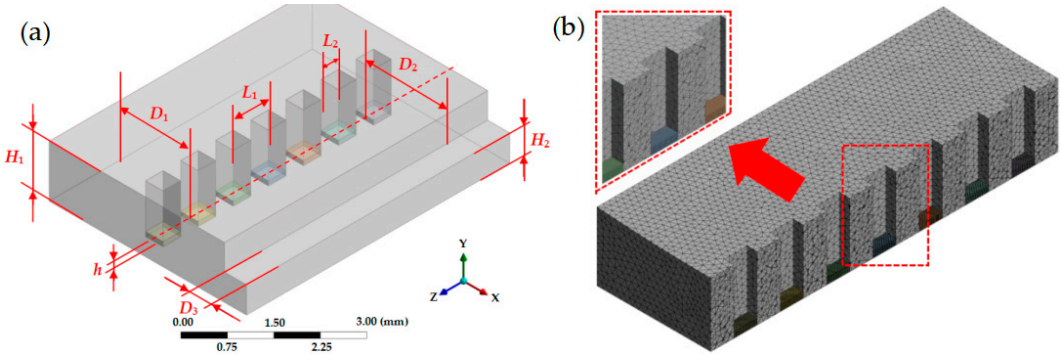


Figure 4. Simulation model. (**a**) Physical model; (**b**) meshed model.

Table 1. Boundary conditions of the numerical model.

Item	Parameter	Unit
Height of outlet [H_1]	1.20	[mm]
Height of inlet [H_2]	0.60	[mm]
Left lateral wall spacing [D_1]	1.80	[mm]
Right lateral wall spacing [D_2]	2.20	[mm]
Entrance side wall spacing [D_3]	0.50	[mm]
Machining gap [h]	100	[μm]
Electrode spacing [L_1]	800	[μm]
Electrode width [L_2]	400	[μm]

4.2. Simulation Analysis

According to the simulation results, after the ultrasonic energy field is applied, the ultrasonic vibration causes the electrolyte to generate intense vibration and acceleration, thereby accelerating the flow velocity of the electrolyte within the machining gap shown in Figure 5c,g. When the vibrating end moves away from the machining surface, the pressure in this region will drop rapidly, forming a local low-pressure area. As a result, the electrolyte continuously flows inwards, and the flow velocity in the regions with the same initial velocity increases in Figure 5b,f. When the vibrating end approaches the machining surface, the electrolyte between them will be strongly compressed, forming a local high-pressure area, which constantly squeezes outwards in Figure 5d,h. The dynamic changes between these local high-pressure and low-pressure areas create an effect similar to "pumping", which helps to discharge the electrolytic products and heat within the machining gap more effectively. Meanwhile, it attracts fresh electrolyte into the gap, maintaining the stability of the machining process.

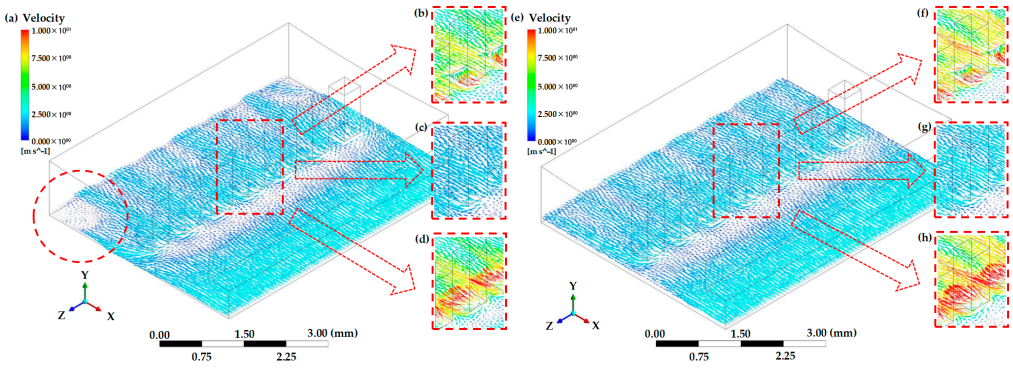


Figure 5. Simulation results. (**a**) Unoptimized; (**e**) Optimized.

However, when the outlet boundary is positioned too close to the flow field region exhibiting complex flow phenomena, unsteady flow features can readily propagate to the outlet, leading to sustained fluctuations in flow field parameters at the outlet section. This instability subsequently destabilizes the entire free outflow domain, potentially creating stagnation zones with near-zero flow velocity, as denoted by the red circle in Figure 5a. Under this operational condition, through streamlined optimization measures—specifically, revising the electrolyte inlet/outlet configuration to a single left-side outlet and implementing sidewall shielding protection—the velocity distribution within the machining gap is significantly homogenized, as illustrated in Figure 5e.

The flow velocity near the sidewalls is increased, and the differences in flow velocity at different positions within the entire machining gap are reduced, tending to be more uniform. Compared with the unoptimized situation, the flow velocity is increased by nearly 15%. This helps the electrolytic products to be carried out of the machining gap more promptly along with the flow of the electrolyte, reducing problems such as insufficient electrolysis caused by chaotic flow directions, and thus ensuring the accuracy and quality of the overall machining process, as shown in Figure 6.

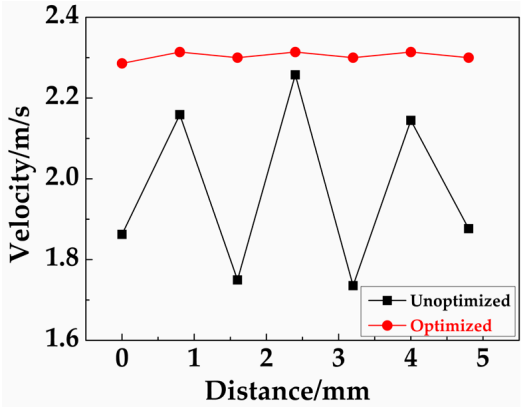


Figure 6. Simulation results of the side-wall flow shielding analysis.

During the micro-electrolytic machining process, the magnitude of the ultrasonic amplitude directly influences the vibration intensity and the resultant effect within the machining gap. Different ultrasonic amplitudes lead to distinct relative motion states between the electrode and the workpiece, which further affects the uniformity of material removal. Through simulation analysis, the material removal conditions in various regions of the machining surface under different amplitudes can be clearly observed. This facilitates the identification of the appropriate amplitude that enables the most uniform material removal, preventing situations where excessive or insufficient material is removed locally [50–52].

As can be seen from Figure 7, when the ultrasonic amplitude is relatively small, the vibration of the electrode within the machining gap is rather weak, and its disturbing effect on the electrolyte is limited. At this time, the electrolyte mainly flows in accordance with the directions set by the conventional inlet and outlet, with a relatively stable and uniform flow velocity. The overall flow velocity value remains at a relatively low level, and its ability to scour and carry away the electrolytic products is also limited. When the amplitude increases, the intense vibration of the electrode will drive the electrolyte to generate a more complex flow. The flow velocity will increase significantly in local areas, forming stronger turbulence, which makes the flow path of the electrolyte within the machining gap more tortuous. Fluent results validate that 35 μm ultrasonic amplitude balances cavitation intensity while avoiding electrode collisions, surpassing UA-EMM's unstable bubble accumulation. The optimized 4 m/s flow velocity (Figure 8) enhances uniformity by 15% versus traditional REMM, addressing the deep-small hole limitation in Liu et al. to

enable planar micro-dimple arrays [34]. This helps to enhance the scouring effect of the electrolyte on the machining area, enabling the timely removal of electrolytic products.

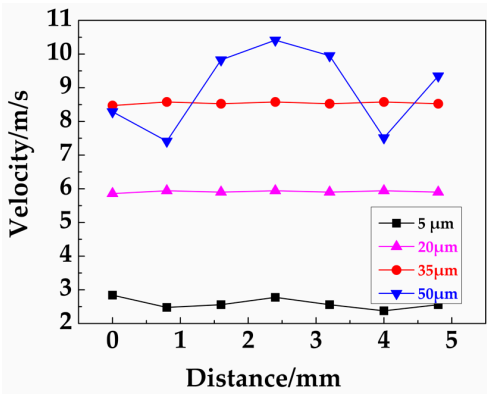


Figure 7. Simulation results of different ultrasonic amplitudes.

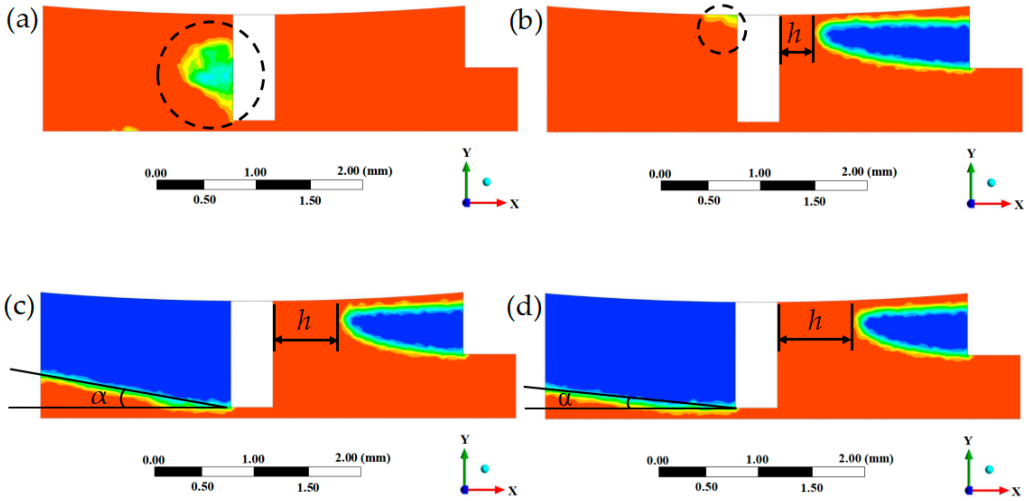


Figure 8. Simulated cloud images at different initial liquid flow velocities. (**a**) 2 m/s, (**b**) 3 m/s, (**c**) 4 m/s, and (**d**) 5 m/s.

However, if the ultrasonic amplitude is too large, the violent vibration of the electrode will cause the flow, pressure, and cavitation of the electrolyte to be in a highly dynamic state. The flow field parameters will fluctuate frequently and with large amplitudes, and unstable factors such as local turbulence out of control and abnormal pressure are likely to occur, which will affect the final machining accuracy. An ultrasonic amplitude of 35 μm was identified as ideal, balancing sufficient cavitation intensity for passive film removal shown in Figure 7 and avoiding excessive electrode–workpiece collisions.

Figure 8 present the cloud images of the cross-sectional flow field distributions under different initial liquid flow velocities. In the figure, the red regions denote the liquid volume fraction, the blue regions represent the gas volume fraction, and the green regions indicate the mixed phase. When the initial liquid flow velocity is 2 m/s, the flow direction of the electrolyte basically remains along the flushing direction, and there are no obvious transverse flows or backflow phenomena on the cross-section. This simple flow direction makes the flow field relatively stable and easy to control during the machining process. However, it may also lead to the situation where some parts of the machining area cannot be fully scoured by the electrolyte, thus affecting the uniformity of the machining, as shown in Figure 8a. This is attributed to the insufficient kinetic energy of the electrolyte at low flow velocity (2 m/s), leading to the formation of stagnant zones where fluid momentum fails to penetrate the entire machining gap. The laminar flow pattern at this velocity

restricts transverse mixing, creating regions with minimal flow where electrolytic products accumulate and current density distributes unevenly. The resulting inadequate electrolyte renewal in these areas hinders anodic dissolution, causing non-uniform material removal, as validated by the flow field simulation showing velocity gradients approaching zero in localized regions. After the liquid flow velocity increases, some transverse flow components and small backflow regions start to appear on the cross-section. Near the machining wall surface, due to the obstruction of the wall, the electrolyte will generate a certain amount of transverse flow, forming local circulation loops. The distance of the side circulation loops is denoted by h. In the central part of the machining area, some small backflow areas may also emerge, making the flow of the electrolyte within the machining area more complex. Such changes in the flow direction are conducive to expanding the coverage range of the electrolyte over the machining area and making the machining more uniform. However, it is necessary to pay attention to controlling the stability of the flow direction to avoid impacts on the machining accuracy, as shown in Figure 8b. Under the effect of the high-speed jet at the flushing end, the distance of h in the mainstream direction from the flushing end to the outlet end increases, and the flow of the electrolyte becomes more impactful and scouring.

In the machining cross-section, the electrolyte can flow rapidly through the machining area along the predetermined direction with a strong momentum. This plays a significantly positive role in carrying away the electrolytic products in a timely manner and generates an outlet cross-section at an angle of α. Meanwhile, it also promotes the electrolyte to diffuse better in the transverse direction, enabling a more uniform coverage of the machining area, as shown in Figure 8c. However, a relatively large liquid flow velocity significantly intensifies the turbulence degree of the flow field in the cross-section within the machining gap. As a result, the angle of α decreases while the distance of h increases. The disorder and chaos of the electrolyte flow are enhanced, and the mutual mixing and collision among different parts of the electrolyte become more frequent, which makes it difficult to control the flow path of the electrolyte within the machining gap and leads to an uneven distribution of the flow velocity. The choice of 4 m/s initial flow velocity is rooted in Fluent simulations (Figure 8), which showed that velocities below 3 m/s led to stagnant zones (Figure 8a), while velocities above 5 m/s induced turbulent flow instabilities (Figure 8d). At 4 m/s, the flow field uniformity index (defined as the ratio of minimum to maximum velocity) reached 0.89, 15% higher than unoptimized conditions. Similarly, 35 μm ultrasonic amplitude was selected because it balanced cavitation intensity and machining stability: amplitudes < 20 μm failed to disrupt passivation layers effectively, while amplitudes > 50 μm caused electrode-workpiece collisions, which predicts optimal gap variation for uniform dissolution. Fluent simulations validated that 4 m/s flow velocity and 35 μm amplitude optimize flow uniformity.

5. Experimental Design

5.1. Experimental Equipment

The principle of the experimental system depicted in Figure 9, which is rather intricate and encompasses multiple key subsystems. Firstly, there is the ultrasonic generation system, which is composed of an ultrasonic generator and a transducer. The generator is capable of generating high-frequency electrical signals. Subsequently, the transducer plays a crucial role in converting these signals into ultrasonic vibrations. This leads to the occurrence of cavitation effects within the electrolyte, thereby significantly enhancing the electrolytic effect. The pulsed power supply system is another vital part. It outputs electrical energy with specific pulse parameters, allowing for precise control over the on–off of current, as well as its amplitude and frequency. This precise control is essential for pulsed electrolysis

and greatly improves the machining precision and quality. The electrolyte circulation system, consisting of a storage tank, pump, filter, and pipes, has its own functions. The storage tank serves as a repository for the electrolyte. The pump undertakes the task of circulating it throughout the system, while the filter is responsible for removing impurities to maintain the purity of the electrolyte. The motion control system relies on motors and lead screws to manage the rotation, translation of the workpiece, and feed of electrodes. This meticulous control ensures the uniformity and accuracy of the machining process. The micro-rolling erosion electrolytic system, equipped with special electrodes and clamping devices, realizes precise material removal and high-quality machining by leveraging the cooperation of the ultrasonic energy field, pulsed power supply, and electrolyte circulation. Moreover, the relevant experiment parameters are clearly listed in Table 2, providing a reference for the whole experimental operation.

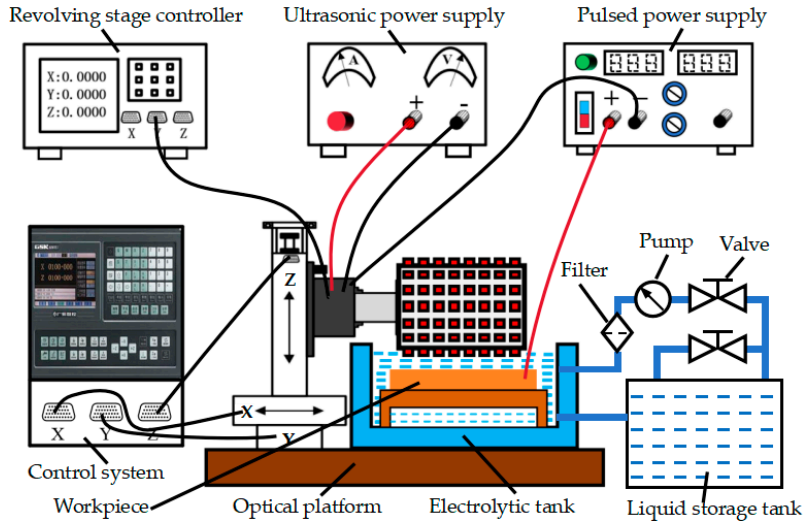


Figure 9. Experimental equipment of RUREMM.

Table 2. Experimental conditions.

Item	Symbol	Value	Unit
Protrusion size	A × A	400 × 400	[μm]
Rotation speed	V_r	0.008	[r/min]
Pulse voltage	U	10	[V]
Pulse frequency	f_1	16	[kHz]
Workpiece diameter	D	50	[mm]
Electrolytic velocity	V_e	2, 3, 4, 5	[m/s]
Ultrasonic amplitude	A	5, 20, 35, 50	[μm]
Inter-electrode gap	Δ	20, 60, 100, 140	[μm]
Electrolyte concentration	wt	10	[%]
Electrolyte temperature	T_e	25	[°C]
Ultrasonic vibration frequency	f_2	28	[kHz]
Machining time	t	5	[min]

5.2. Experimental Setup

The processing experiments consist of three main parts. Firstly, a high-speed camera (Keyence VW6000 from Keyence Corporation, located in Osaka, Japan) was used to capture

the distribution of bubble clusters in the machining gap before and after applying the ultrasonic energy field. Analysis showed that this field could generate cavitation and micro-jets, making tiny bubbles form clusters. Secondly, the formation morphology laws of micro-pits in micro-rolling erosion electrolytic machining were analyzed and compared before and after ultrasound application. The depth-to-width ratio of micro-pits increased, contours became clearer, and stray corrosion reduced after applying the ultrasonic energy field, verifying the feasibility of REMM in it. Thirdly, the formation laws of pitting pits at different times before and after the ultrasonic energy field's action were analyzed. Results indicated that the field could suppress or remove the passive film on the workpiece surface and enhance the reaction speed of micro-electrolytic machining. Finally, the influence of machining parameters (machining gap, ultrasonic amplitude, liquid flow rate) was investigated. Optimal parameters were obtained, and an array of micro-pits with a width of 223.4 μm, a depth of 28.9 μm, a depth-to-width ratio of 0.129, a surface roughness of 0.205 μm, minimal stray corrosion, and good surface quality was fabricated.

5.3. Experiment on Bubble Observation

The electrolyte stream is directed toward the machining zone through the nozzle. In conventional roll imprinting electrolytic machining (REMM) without ultrasonic energy field excitation, substantial quantities of relatively large bubbles erupt from the machining gap, exhibiting a sparse and non-uniform distribution pattern, as depicted in Figure 10a. This operational state is characterized by a narrow machining gap, which inherently restricts electrolyte renewal efficiency. Consequently, electrolytic byproducts and particulates generated during the machining process accumulate within the gap, while frictional heat dissipation is severely impeded. These combined factors give rise to critical issues, including diminished machining productivity and unstable material removal dynamics. In contrast, when an ultrasonic energy field is integrated into the roll imprinting electrolytic machining system shown in Figure 10b, the post-machining observation reveals the formation of dense, homogeneously distributed white bubble clusters within the inter-electrode gap. The imposed ultrasonic cavitation effect induces significant modifications to the gap flow field: it enhances electrolyte circulation velocity, facilitating the timely evacuation of reaction products and bubble aggregates in the enlarged red circles. Mechanistically, ultrasonic waves induce resonant oscillations in electrolytic bubbles nucleated at the tool electrode surface, disrupting their adherence to the electrode interface. This promotes continuous detachment of micro-bubbles, which then rapidly coalesce into larger bubble clusters that rise to the liquid surface. The resultant improvement in mass and heat transfer within the machining gap effectively mitigates the drawbacks associated with conventional REMM.

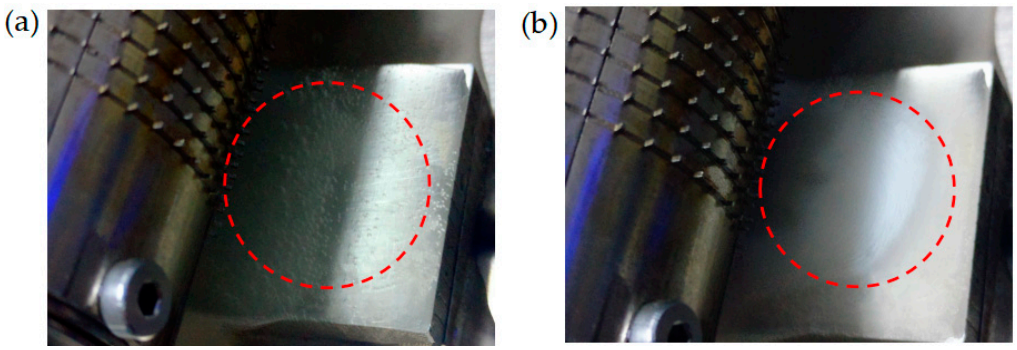


Figure 10. Bubble change diagram. (**a**) REMM; (**b**) RUREMM.

Figure 11 illustrates the experimental setup for photographing bubbles. The lens of the high-speed camera was aligned with the machining gap, and the tool cathode was closely attached to the glass slide to facilitate a clear observation of the bubble conditions inside the gap. Then, careful focusing was carried out, followed by recording and photographing, aiming to analyze the laws governing the generation and distribution of bubbles before and after the action of the ultrasonic energy field.

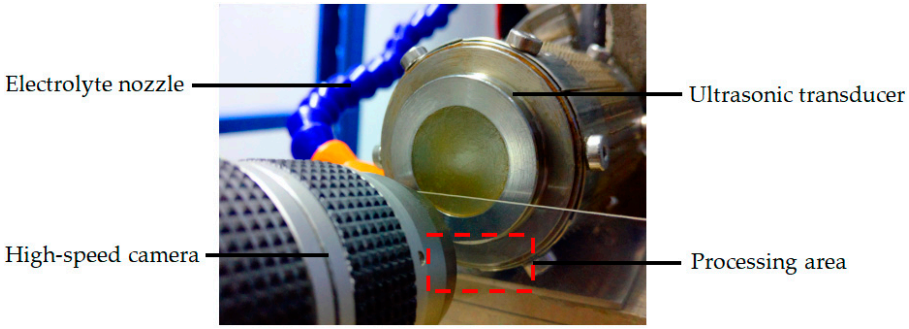


Figure 11. Schematic diagram of the bubble imaging device.

A comparative analysis of bubble imaging results was carried out. Figure 12a shows the motion and distribution of bubbles in roll imprinting electrolytic machining. Influenced by atmospheric pressure and electrolyte flow rate, generated bubbles follow the flow direction and diffuse towards the liquid surface. During machining, continuously produced bubbles accumulate into large ones as they cannot diffuse in a timely manner. In contrast to conventional REMM, where electrolyte stagnation and passive film buildup often compromise machining precision, RUREMM leverages ultrasonic-induced micro-jets to disrupt bubble coalescence and enhance electrolyte renewal, as validated by high-speed photography shown in Figure 12b, which presents the situation under the same machining with an ultrasonic energy field in the enlarged red circles. Due to its application, cavitation occurs in the gap, generating high-velocity micro-jets. Thus, bubbles rapidly diffuse and leave the area before growing larger. Compared to without the ultrasonic field, bubble size is significantly reduced and distribution is more uniform, resulting in uniform current density, less stray corrosion, improved localization, and better machining quality.

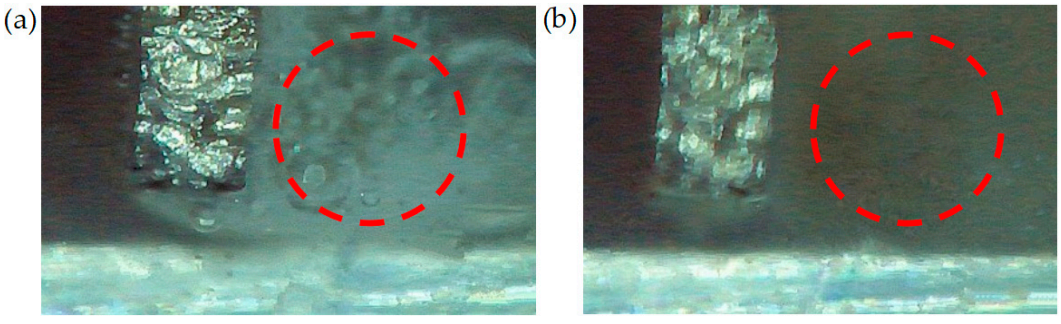


Figure 12. Photograph of bubbles in the machining gap. (**a**) REMM; (**b**) RUREMM.

To explore the mechanisms governing material corrosion, Figure 13 displays scanning electron microscopy (SEM) images of anodically dissolved surface structures at distinct machining times during the RUREMM process. At a machining time of 0.1 s, a passive layer spontaneously forms on the workpiece surface during micro-electrolytic machining in the enlarged red circle. This layer impedes anodic metal dissolution, induces localized corrosion, decreases the reaction rate, and restricts processing efficiency, as shown in Figure 13a. Upon introduction of the ultrasonic energy field, the cavitation effect generates

intense shockwaves through bubble collapse, which effectively peels off the passive layer and creates minute pits on the surface. At 0.2 s, although the corrosion rate increases in the conventional REMM (Figure 13c), electrochemical reactions remain heterogeneous across the surface. In contrast, the ultrasonic-assisted RUREMM promotes a uniformly distributed reaction over the entire surface. The continuous micro-jet impacts from ultrasonic cavitation lead to the formation of dense, fine pits, as shown in Figure 13d. When the machining time extends to 2.0 s, disordered corrosion patterns persist in the non-ultrasonic condition (Figure 13e). However, in the ultrasonic-enhanced process, the combined effects of powerful shockwaves and micro-jets enable more uniform scouring of the electrolyte across the surface. This action mitigates ion concentration gradients, prevents excessive localized electrolysis, enhances edge fluid flow, and homogenizes the electric field distribution. As a result, the edge effect is mitigated, the variability in pit distribution is reduced, and the overall precision of micro-electrolytic machining is significantly improved, as shown in Figure 13f.

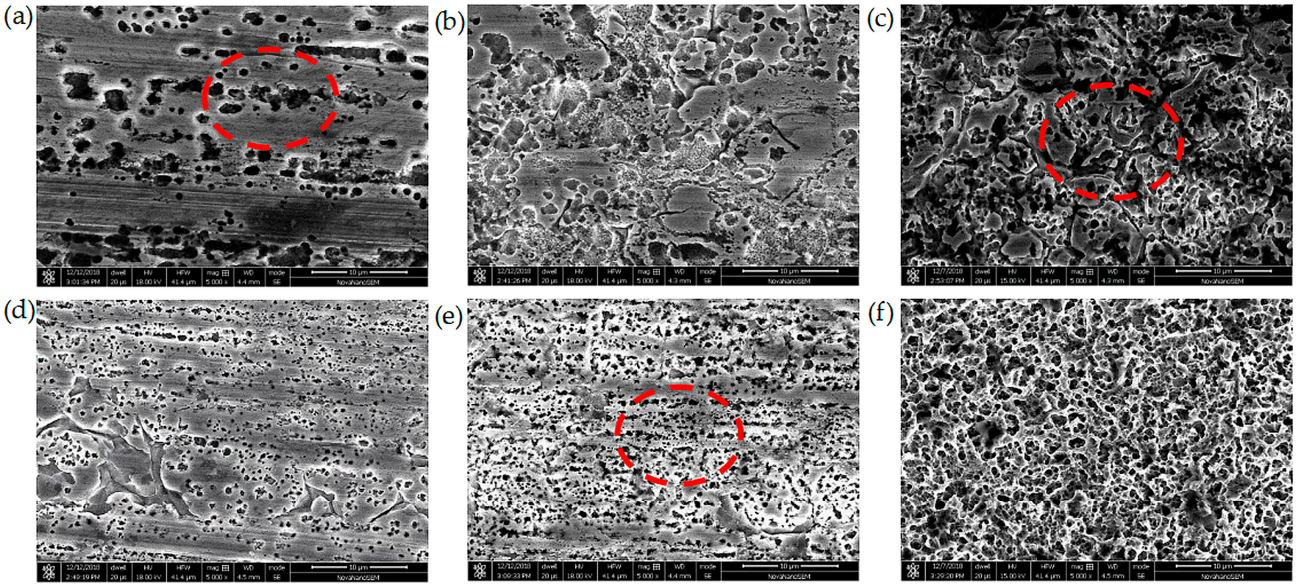


Figure 13. SEM images of surface structures anodically dissolved at different times, REMM: (**a**) 0.1 s, (**c**) 0.2 s, (**e**) 2.0 s; RUREMM: (**b**) 0.1 s, (**d**) 0.2 s, (**f**) 2.0 s.

5.4. Effect of Different Machining Parameters

The dimensions and morphologies of the micro-pits obtained by REMM and RUREMM stimulated by the ultrasonic energy field were measured and compared. The depth-to-width ratio was calculated, and the stability and consistency of the array of micro-pits during machining were analyzed. Moreover, the influence of machining parameters (machining gap, ultrasonic amplitude, and liquid flow rate) on the machining results was investigated. Finally, the machining law curves were plotted and analyzed. An appropriate machining gap is conducive to maintaining a stable machining state and ensuring the consistency between the shape of the workpiece's machined surface and that of the tool electrode; the relevant analysis table regarding the influence of ultrasonic amplitude on pit size is shown in Table 3. Parameters were selected based on Fluent simulations of flow field uniformity (Section 4) and experimental verification of bubble distribution and surface roughness (Section 5.3), ensuring minimal stray corrosion and maximal dimensional accuracy.

Table 3. Analysis table regarding the influence of machining gap on pit size.

Items	Machining Gap [μm]	Short Circuits	Width [μm]	Depth [μm]	Aspect Ratio
REMM	20	2	384.5	16.15	0.0420
	60	0	351.6	18.96	0.0539
	100	0	312.9	17.65	0.0564
	140	0	221.2	9.91	0.0448
RUREMM	20	4	281.1	14.51	0.0516
	60	0	260.5	22.48	0.0863
	100	0	227.2	20.62	0.0908
	140	0	211.3	15.63	0.0740

When the machining gap is appropriate, the electrolytic process can proceed smoothly and uniformly, as shown in Figure 14. Materials can be removed regularly at the microscopic level, and situations like excessive material corrosion and unevenness caused by abnormal local current density will not occur, thus making the workpiece surface relatively smooth and flat. However, if the gap is too small, it is prone to cause a short circuit between the tool electrode and the workpiece. Instantly, a relatively large current impact will be generated, which may not only damage the electrode and the workpiece but also force the entire machining process to be interrupted. It is necessary to readjust before continuing, as shown in Table 3. When the machining gap is too large, it tends to result in uneven current distribution, triggering local abnormal electrolytic reactions and forming microscopic pits on the workpiece surface, etc. This will increase the surface roughness and have an impact on the surface quality.

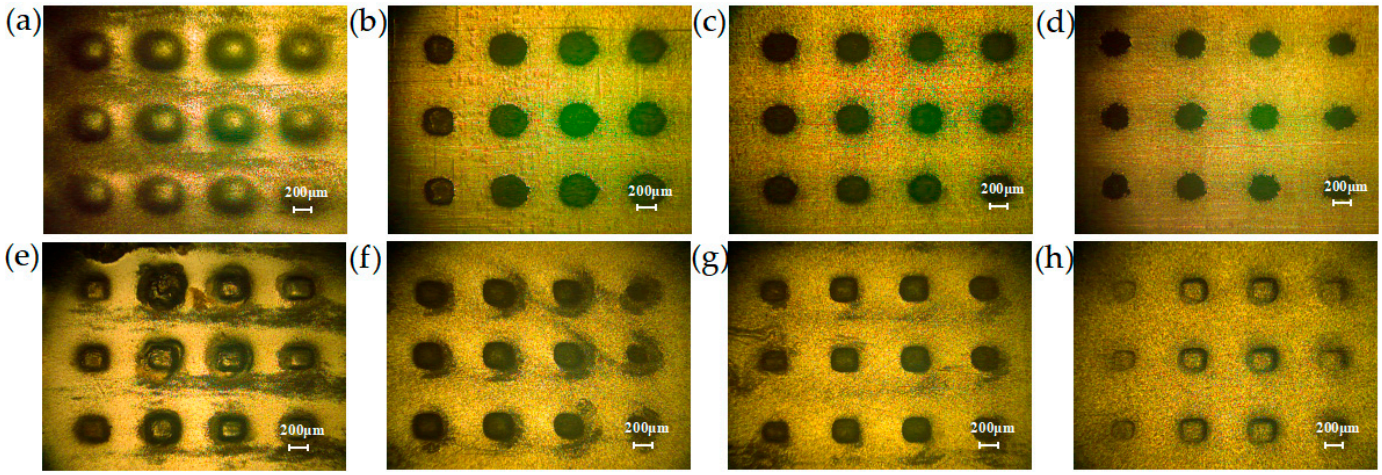


Figure 14. Morphology of the array of the micro-pits under different machining gaps (μm), REMM: (**a**) 20, (**b**) 60, (**c**) 100, (**d**) 140; RUREMM: (**e**) 20, (**f**) 60, (**g**) 100, and (**h**) 140.

An appropriate machining gap enables the electrolytic process to proceed stably and uniformly. Microscopically, materials can be regularly removed without excessive corrosion or unevenness due to abnormal local current density, resulting in a relatively smooth workpiece surface. However, a too-narrow gap may cause a short circuit between the tool electrode and the workpiece, generating a large current impact instantaneously. This can damage both the electrode and the workpiece and interrupt the machining process, which requires readjustment (as shown in the table). Conversely, an overly large gap leads to uneven current distribution, causing local abnormal reactions and microscopic pits on the workpiece surface, increasing surface roughness and degrading surface quality. After

applying the ultrasonic energy field, the micro-jets and impact forces from the cavitation effect act uniformly on the workpiece surface, removing microscopic protrusions and burrs, thus making the surface smoother and reducing roughness (Figure 14f,g).

When the machining gap is relatively small, the ultrasonic energy field is applied, which makes the process highly unstable. Frequent abnormal collisions between the tool electrode and the workpiece can cause significant variations in depth across regions. In some areas, excessive impact leads to over-removal; in others, electrode deviation results in insufficient removal. Overall, it is hard to achieve a uniform depth meeting design requirements (Figure 14a). Excessively violent vibrations easily trigger faults like short circuits. Once a short circuit occurs, electrolytic machining halts, unable to increase depth and potentially damaging the workpiece and electrode, aborting the machining and failing to meet the depth requirements shown in Figure 14e.

As revealed by the corresponding size analysis of Figure 15, upon the application of the ultrasonic energy field, the width of the micro-pits is significantly decreased while the depth is increased. The underlying reason is that the ultrasonic energy field is capable of effectively agitating and scouring the electrolyte, thus expediting the rapid removal of electrolytic products from the machining gap and averting their accumulation at the boundaries of the machining area. Specifically, when the machining gap is set at 100 μm, the width of the micro-pits generated by RUREMM is approximately 27.4% less than that generated by REMM. Meanwhile, the depth is increased by around 16.8%, and the depth-to-width ratio is enhanced by approximately 61.0%. Moreover, compared to the situation where the initial machining gap is 20 μm, the depth-to-width ratio is increased by about 76.0%.

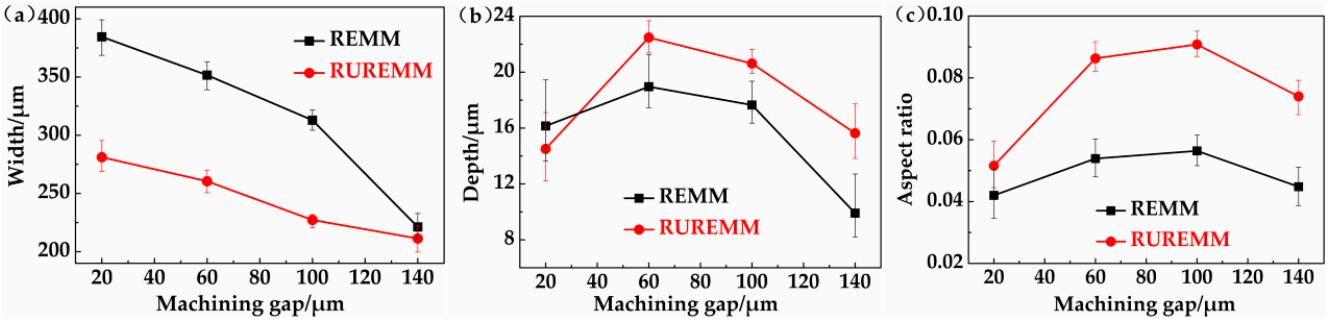


Figure 15. Effects of machining gaps on array pit dimensions during REMM and RUREMM. (**a**) Width; (**b**) depth; (**c**) aspect ratio.

In the process of micro-electrolytic machining, an appropriate ultrasonic amplitude is beneficial for enhancing the surface integrity. With rational vibration, electrolytic products can be promptly discharged, which prevents them from accumulating on the workpiece surface and thus forming defects such as pits. At the same time, a stable machining process can preclude issues like micro-cracks and spalling that are induced by violent vibrations. The relevant data are presented in Table 4. When the ultrasonic amplitude is too small, it cannot effectively break the passive film or discharge electrolytic products promptly. Hence, electrolytic reactions may continue at boundaries, blurring them, reducing width and size precision, and limiting machining depth.

Nevertheless, the intense and uneven forces generated by a relatively large ultrasonic amplitude will give rise to substantial differences in material removal at various positions. Furthermore, an unstable machining process might result in excessive removal of local materials, short circuits, and other adverse circumstances. As a consequence, the surface texture becomes rough and irregular, with the direction, density, and depth of the texture lacking consistency and presenting a chaotic appearance, as shown in Figure 16d.

Table 4. Analysis table regarding the influence of ultrasonic amplitude on pit size.

Items	Amplitude [μm]	Short Circuits	Width [μm]	Depth [μm]	Aspect Ratio
RUREMM	5	0	275.5	17.91	0.0650
	20	0	227.2	20.62	0.0908
	35	0	211.9	23.62	0.1115
	50	3	204.6	15.54	0.0760

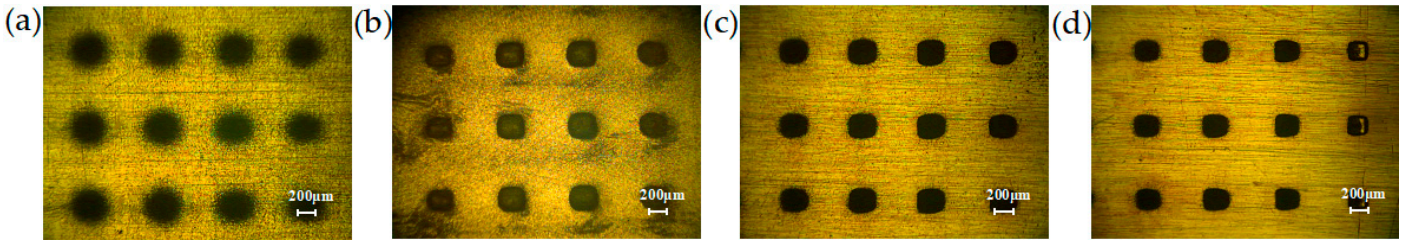


Figure 16. Morphology of array of the micro-pits under different ultrasonic amplitudes (μm): (**a**) 5; (**b**) 20; (**c**) 35; (**d**) 50.

It can be observed from the corresponding size diagrams that as the ultrasonic amplitude increases, the width of the micro-pits tends to decrease gradually, while the depth increases accordingly in Figure 17. Nevertheless, when the ultrasonic amplitude reaches 50 μm, a significant reduction in the depth of the micro-pits occurs. The reason for this lies in the fact that when the amplitude becomes excessively large, the contact between the tool electrode and the workpiece turns out to be extremely unstable, giving rise to frequent abnormal collisions. Consequently, there are substantial disparities in the amount of material removed across different regions. In some areas, the depth far exceeds expectations, whereas in others, it falls short, which leads to a considerable depth deviation and makes it challenging to fulfill the precision requirements regarding the depth-to-width ratio in machining. Based on the above analysis, upon adopting an ultrasonic amplitude of 35 μm, the width of the array micro-pits is decreased by approximately 23.1%, the depth is increased by 31.9%, and the depth-to-width ratio is enhanced by 71.5%.

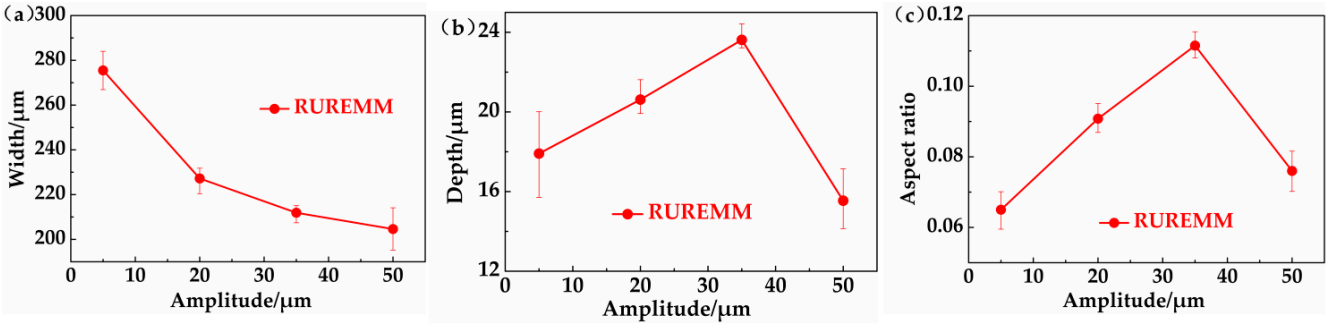


Figure 17. Effects of ultrasonic amplitude on array pit dimensions during RUREMM. (**a**) Width; (**b**) depth; (**c**) aspect ratio.

In REMM, the electrolyte flow rate exerts a remarkable influence on the surface topography of the workpiece; the relevant data are presented in Table 5. When the flow rate is relatively low, it becomes arduous for the electrolytic products to be removed promptly. Subsequently, these products accumulate within the machining area, rendering it difficult to precisely control the machining width and making the boundaries liable to become blurred. Additionally, the machining depth increases at a sluggish and uneven pace as a

result of the reaction being hampered. Meanwhile, such accumulations will also render the workpiece surface rougher, undermine its surface integrity, and have an adverse impact on the surface quality in Figure 18. Conversely, as the electrolyte flow rate rises, it is capable of swiftly removing the electrolytic products. As a consequence, the machining width can be controlled with greater precision, the boundaries become distinct, and the increase in depth is expedited, which is conducive to fulfilling the anticipated depth requirements. Moreover, a high flow rate can maintain a cleaner workpiece surface, make the electrolytic reaction more uniform, effectively reduce the surface roughness, and enhance the surface quality.

Table 5. Analysis table regarding the influence of flow velocity on pit size.

Items	Flow Velocity [m/s]	Short Circuits	Width [μm]	Depth [μm]	Aspect Ratio
REMM	2	2	280.6	13.59	0.0484
	3	0	312.9	17.65	0.0564
	4	0	321.6	18.98	0.0590
	5	0	333.4	19.15	0.0574
RUREMM	2	1	203.6	21.55	0.1058
	3	0	211.9	23.62	0.1115
	4	0	223.4	28.89	0.1293
	5	0	230.5	29.26	0.1269

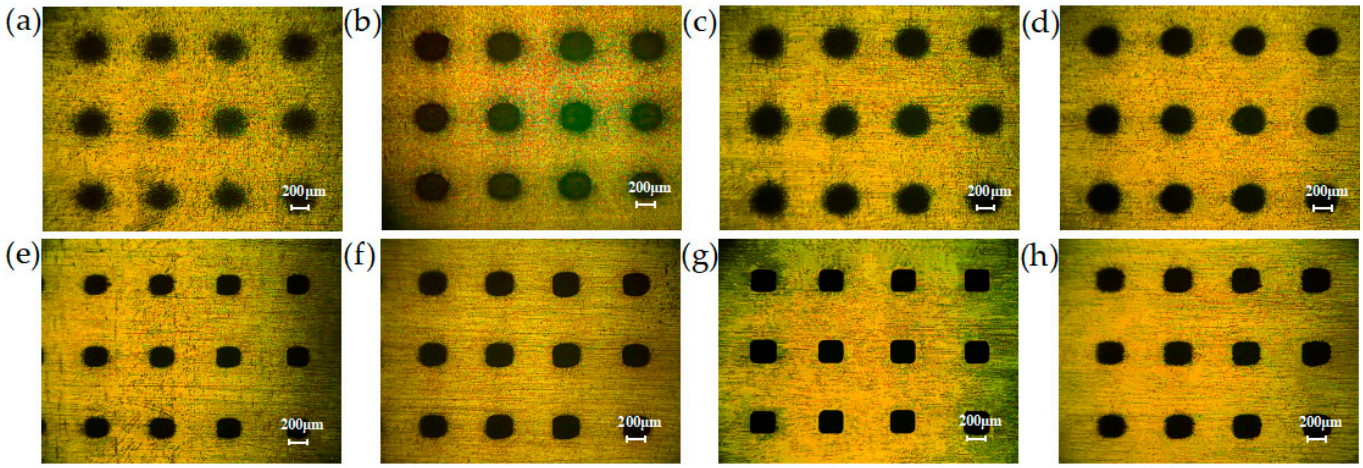


Figure 18. Morphology of array of the micro-pits under different flow velocity (μm), REMM: (**a**) 20, (**b**) 60, (**c**) 100, (**d**) 140; RUREMM: (**e**) 20, (**f**) 60, (**g**) 100, and (**h**) 140.

Nonetheless, if the flow rate is excessively high, it may exert an impact on the workpiece surface and give rise to local damage. Hence, it is essential to reasonably regulate the electrolyte flow rate so as to ensure an ideal surface topography of the workpiece. The ultrasonic energy field has the ability to fracture the passive film on the workpiece surface, which allows the electrolytic reaction to occur in a more comprehensive and profound manner. This, in turn, expedites the material removal procedure and effectively augments the machining depth, thus having an impact on the depth-to-width ratio. Furthermore, the micro-jets produced by the ultrasonic energy field possess the capacity to eliminate microscopic protrusions on the surface. This leads to a reduction in the surface roughness and renders the surface smoother. In addition, it can also promote the uniform flow of the electrolyte, mitigate local abnormal electrolysis, and improve the surface integrity shown in Figure 18f,g.

It can be observed from the data size analysis diagram in Figure 19 that as the electrolyte flow rate increases, the width and depth of the array micro-pits continue to grow.

Nevertheless, the depth-to-width ratio calculated by REMM remains nearly constant, whereas that of RUREMM experiences a gradual increase. This is attributable to the fact that the cavitation effect generated by the ultrasonic energy field can promote in-depth electrolysis, augment the machining depth, and consequently exert an influence on the depth-to-width ratio. Simultaneously, the micro-jets within the energy field are capable of enhancing the surface quality and reducing the surface roughness. With an increasing flow rate, the products can be promptly removed, which facilitates more precise control over the width and ensures a more stable increase in depth. When these two aspects work in concert, optimizing the parameters in a rational manner can improve the surface topography of the workpiece, boost the surface quality, and render the surface flatter and smoother. Based on the above analysis, upon adopting a liquid flow rate of 4 m/s, the width is increased by approximately 9.7%, the depth is increased by 34.1%, and the depth-to-width ratio is enhanced by 22.2%. As a result, an array of micro-pit topography with higher surface precision can be achieved. These findings demonstrate a significant improvement in depth-to-width ratio compared to conventional REMM, where the ratio remains nearly constant (Table 5). The enhancement can be attributed to the ultrasonic-induced cavitation effect, which promotes deeper anodic dissolution by disrupting passivation layers—a consistent observation. In contrast, our study uniquely integrates ultrasonic amplitude (35 μm) and flow velocity (4 m/s) to balance material removal uniformity and depth, addressing a limitation in previous work where high amplitude often caused unstable machining.

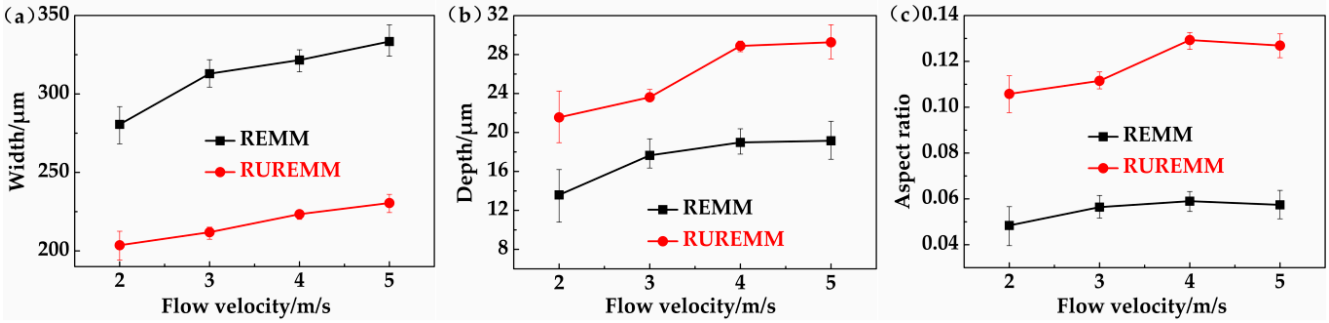


Figure 19. Effects of flow velocity on array pit dimensions during REMM and RUREMM. (**a**) Width; (**b**) depth; (**c**) aspect ratio.

Under the optimized processing parameters—rolling erosion speed of 0.008 r/min, pulse voltage of 10 V, pulse frequency of 16 kHz, machining gap of 100 μm, electrolyte flow rate of 4 m/s, ultrasonic amplitude of 35 μm, and electrolyte concentration of 10%—the SEM surface topography is illustrated in Figure 20. Cross-sectional dimensions were characterized using a three-dimensional profilometer. Measurement results indicate that the array micro-pits exhibit an average width of 223.4 μm, a mean depth of 28.90 μm, a depth-to-width ratio of approximately 0.129, and a surface roughness (Ra) of 0.205 μm. Significantly, the micro-pits feature well-defined contours, with a notable reduction in stray corrosion and a more uniform material removal process. Experimental results showed that RUREMM achieved micro-pits, outperforming traditional REMM by 61% in aspect ratio and 58% in surface smoothness. Moreover, future research will include the following: (1) extending RUREMM to titanium alloys and other high-strength metals to explore material adaptability; (2) investigating the synergistic effect of multi-frequency ultrasonic fields on flow field uniformity and micro-pit aspect ratio control; (3) integrating in situ electrochemical impedance spectroscopy for real-time monitoring of passivation layer dynamics; and (4) applying RUREMM to fabricate hierarchical micro-nano textures for enhanced tribological performance in aerospace components, thus advancing its engineering utility.

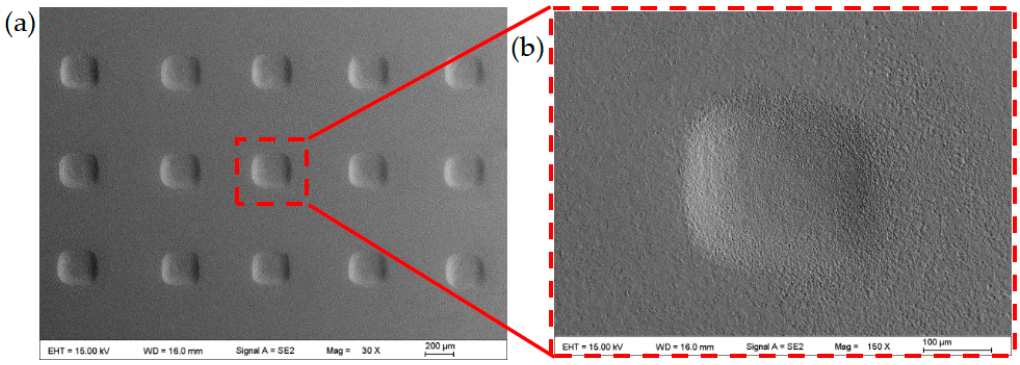


Figure 20. The diagram of experimental results with optimized parameters. (**a**) Whole view; (**b**) enlarged view.

6. Conclusions

In this paper, the relevant mathematical model was established, and the flow field within the narrow electrolytic machining gap of the ultrasonic energy field was analyzed and optimized through Fluent software. The experiment on bubble observation was studied, and the effect on micro-pit morphology formation was analyzed at different times. Analyze the laws governing the formation of pitting pits in RUREMM at different times and explore the impact of the ultrasonic energy field on micro-electrolytic machining. Moreover, appropriate machining parameters can improve the localization and surface quality of micro-dimples in RUREMM; the relevant conclusions are as follows:

(1) A theoretical model was developed to quantify ultrasonic-electrochemical coupling in rotary ultrasonic-assisted reverse electrochemical machining (RUREMM). CFD simulations demonstrated sidewall shielding optimized electrolyte flow homogeneity, achieving laminar stability at 4 m/s and 35 µm. Critical parameters for minimizing machining fluctuations were identified. Future work includes multi-physics modeling with thermal stress effects, AI-driven adaptive control, and nano-electrolyte integration to enhance material removal. Applications span aerospace turbine blade fabrication, medical implant surface engineering, and microelectronics via drilling, addressing precision manufacturing needs for advanced materials with a reduced environmental footprint.

(2) High-speed imaging of machining gap bubble dynamics revealed ultrasonic suppression of coalescence, reducing cluster size, while cavitation-induced micro-jets modulated flow field behavior. CFD modeling validated optimal parameters at 20 kHz, 35 µm amplitude, and 4 m/s electrolyte flow. Future work focuses on multi-physics integration of bubble-electrochemical interactions, AI-driven real-time monitoring systems, and nano-electrolyte formulations to enhance cavitation efficiency. Applications include aerospace titanium alloy finishing, medical implant surface microstructuring, and semiconductor precision etching, addressing sub-µm precision demands in advanced manufacturing via ultrasonic cavitation control.

(3) Analysis of metal surface pitting formation dynamics revealed that ultrasonic energy fields disrupt passive film formation during micro-electrolytic machining via combined mechanical–chemical effects, while enhancing electrolyte renewal, product discharge, and material erosion rates. Future work could focus on developing real-time passive film monitoring techniques using electrochemical impedance spectroscopy, optimizing ultrasonic parameters through machine learning to control material removal rates, and exploring hybrid processes integrating ultrasonic vibration with abrasive particles for enhanced surface finishing. This research has potential applications in aerospace for turbine blade repair, automotive for precision machining of engine

components, and marine engineering for corrosion-resistant surface modification of ship hulls, addressing industrial needs for high-precision, environmentally friendly metal processing technologies.

(4) Micro-dimple arrays were fabricated on SS304 via rotary ultrasonic-assisted reverse electrochemical machining (RUREMM), achieving 223.4 μm width and 28.90 μm depth dimples with a 0.129 aspect ratio and Ra 0.205 μm—outperforming traditional ECM. Ultrasonic micro-jets and homogenized flow fields suppressed stray corrosion and bubble unevenness, enabling this advancement. Key parameters included 35 μm amplitude, 4 m/s electrolyte flow, and optimized machining gap. Future work focuses on in situ monitoring systems, AI-driven parameter optimization for dimple consistency, and hybrid ultrasonic-nanoparticle electrolytes to enhance MRR. Applications span aerospace turbine blade texturing, automotive piston ring lubrication enhancement, and biomedical implant osseointegration, addressing high-precision microfabrication demands for defect-free metal components.

Author Contributions: Conceptualization, W.T. and L.L.; tables and figures generation, W.T. and L.L.; article identification, screening, retrieval, selection, and analysis, W.T. and L.L.; review and editing, W.T.; formal analysis and investigation, L.L.; writing original draft preparation, W.T. and L.L.; supervision, L.L. All authors have read and agreed to the published version of the manuscript.

Funding: This work was supported in part by the Scientific Research Project of the Education Department of Zhejiang Province under Grant No. Y202455485, and the Fundamental Research Funds for the Provincial Universities of Zhejiang (RF-A2024001).

Data Availability Statement: Data are contained within the article.

Conflicts of Interest: The authors declare no conflicts of interest.

Nomenclature

Item	Symbol	Unit
Radial Electrochemical Micromachining	REMM	
Radial Ultrasonic Rolling Electrochemical Micromachining	RUREMM	
Electrical and liquid constants of electrochemical machining	$\eta\omega\sigma U_R$	
Vibration velocity component along the *X*-axis	V_X	[m/s]
Vibration velocity component along the *Y*-axis	V_y	[m/s]
Initially set electrode gap	Δ_Z	[μm]
One point within the energization time region [t_1, t_2]	ξ	[min]
Material removal speed of workpiece	$v(t)$	[mm/min]
Period of ultrasonic vibration	T	[min]
Height of outlet	H_1	[mm]
Height of inlet	H_2	[mm]
Left lateral wall spacing	D_1	[mm]
Right lateral wall spacing	D_2	[mm]
Entrance side wall spacing	D_3	[mm]
Machining gap	h	[μm]
Electrode spacing	L_1	[μm]
Electrode width	L_2	[μm]
Angle between the cross-section and the horizontal plane	α	[°]
Protrusion size	A × A	[μm]
Rotation speed	V_r	[r/min]
Pulse voltage	U	[V]
Pulse frequency	f_1	[kHz]

Workpiece diameter	D	[mm]
Electrolytic velocity	V_e	[m/s]
Ultrasonic amplitude	A	[μm]
Inter-electrode gap	Δ	[μm]
Electrolyte concentration	wt	[%]
Electrolyte temperature	T_e	[°C]
Ultrasonic vibration frequency	f_2	[kHz]
Machining time	t	[min]

References

1. Monteiro, P.L.; Labiapari, W.S.; Da Silva, W.M., Jr.; Costa, H.L. Durability of deterministic textures produced by maskless electrochemical texturing (MECT) during Skin pass cold rolling. *Wear* **2025**, *562–563*, 205638. [CrossRef]
2. Xu, P.; Li, Q.H.; Wang, C.Y.; Li, L.; Tan, D.P.; Wu, H.P. Interlayer healing mechanism of multipath deposition 3D printing models and interlayer strength regulation method. *J. Manuf. Process.* **2025**, *141*, 1031–1047. [CrossRef]
3. George, A.; Dhanish, P.B.; Mathew, J. Wear characteristics of WS2 nanoparticle-assisted micro-EDM textured carbide inserts during machining of Ti6Al4V. *Tribol. Int.* **2024**, *195*, 109640. [CrossRef]
4. Yuan, J.; Gastaldi, C.; Goy, E.D.; Chouvion, B. Friction damping for turbomachinery: A comprehensive review of modelling, design strategies, and testing capabilities. *Prog. Aerosp. Sci.* **2024**, *147*, 101018. [CrossRef]
5. Li, L.; Xu, P.; Li, Q.H.; Yin, Z.C.; Zheng, R.Y.; Wu, J.F.; Bao, J.J.; Qi, H.; Tan, D.P. Multi-field coupling particle flow dynamic behaviors of the microreactor and ultrasonic control method. *Powder Technol.* **2025**, *454*, 120731. [CrossRef]
6. Franca, P.H.P.; Barbosa, L.M.Q.; Fernandes, G.H.N.; Machado, A.R.; Martins, P.S.; da Silva, M.B. Internally cooled tools: An eco-friendly approach to wear reduction in AISI 304 stainless steel machining. *Wear* **2024**, *554–555*, 205490. [CrossRef]
7. Ahmed, A.; Masjuki, H.H.; Varman, M.; Kalam, M.A.; Habibullah, M. An overview of geometrical parameters of surface texturing for piston/cylinder assembly and mechanical seals. *Meccanica* **2016**, *51*, 9–23. [CrossRef]
8. Xiao, N.; Khonsari, M.M. Thermal performance of mechanical seals with textured side-wall. *Tribol. Int.* **2012**, *45*, 1–7. [CrossRef]
9. He, T.; Xu, L.; Zhang, N.; Sun, Y.B.; Qi, Y.Z.; Wu, F.H. A superspreading bioinspired micro-texture with the function of self-priming liquid for enhancing boiling heat transfer of cutting-fluid on tool surface. *J. Manuf. Process.* **2025**, *133*, 556–565.
10. Chin, C.H.; Tien-Li, C.; Yen-Cheng, C.; Chien-Ping, W. Enhancing boiling heat transfer by ultrafast laser texturing of groove structures on thin-film graphene surfaces. *Therm. Sci. Eng. Prog.* **2025**, *61*, 103510. [CrossRef]
11. Chen, X.; Rong, Y.; Yang, R.; Wang, M.Z.; Tao, Y.X.; Huang, Y. Graphical compensation of area coverage and stitching accuracy for galvanometric laser texturing on spherical surface. *J. Manuf. Process.* **2025**, *134*, 14–28. [CrossRef]
12. Butler-Smith, P.; Burtt, N.; See, T.L. The friction of surface textured cylinder liner segments modified by Direct Laser Writing and Direct Laser Interference Patterning processes. *J. Manuf. Process.* **2024**, *117*, 366–374. [CrossRef]
13. Jeon, J.H.; Choi, J.Y.; Kim, G.Y.; Kim, G.Y.; Hong, S.J.; Callanga, J.; Lee, C.; Gries, T.; Ahn, S.H. Effect of laser texturing and thermomechanical joining parameters on bond strength of steel-flax fiber reinforced vitrimer composites. *J. Manuf. Process.* **2024**, *124*, 212–225. [CrossRef]
14. Kumar, A.; Ramadas, H.; Kumar, C.S.; Nath, A.K. Laser polishing of additive manufactured stainless-steel parts by line focused beam: A response surface method for improving surface finish. *J. Manuf. Process.* **2025**, *133*, 1310–1328. [CrossRef]
15. Kumar, H.; Roy, T.; Jha, S. Influence of gaseous dielectrics on the wettability of Al-6061 alloy using dry μ-electrical discharge milling. *Appl. Surf. Sci.* **2025**, *685*, 162004. [CrossRef]
16. Yimiao, Z.; Mingbo, Q.; Hui, L.; Yingmin, W.; Jingtao, L.; Zhaowei, L.; Yifan, D.; Cheng, H. Processing of gallium oxide crystals using liquid-immersion wire-cut electrical discharge machining. *Mater. Sci. Semicond. Process.* **2025**, *186*, 109049. [CrossRef]
17. Gao, Q.; Li, K.-L.; Qin, L.; Zhang, Y.O.; Xi, X.C.; Zhao, W.S. A discharge plasma regulation method with spike current for electrical discharge machining. *J. Manuf. Process.* **2024**, *125*, 402–411. [CrossRef]
18. Morovatdel, M.; Osguei, A.T.; Üstünel, Y.C.; Üstünel, Y.C.; Oliaei, S.N. Characterization of micro-wire electrical discharge machining surface texture by empirical mode decomposition. *Measurement* **2025**, *242*, 116184–116189. [CrossRef]
19. Sivashankar, N.; Thanigaivelan, R.; Selvarajan, L.; Venkataramanan, K. Investigation of electrochemical micromachining on magnesium alloy using hollow tool electrode. *Ultrasonics* **2025**, *147*, 107526. [CrossRef] [PubMed]
20. Fang, M.; Hou, L.L.; Yu, L.; Chu, X.F.; Cheng, X.; Wang, J.L. Research on simulation method of multiple time scales dissolution process in tube electrode pulse electrochemical machining. *J. Manuf. Process.* **2024**, *110*, 318–330. [CrossRef]
21. Bhanumathy, S.; Prasanth, B.M.; Anitha, B.; Mohanakanna, R.; Nandhakumar, E.; Hariharan, P. Prediction of material removal rate of SS304 alloy in electrochemical micromachining using machine learning. *Mater. Today Proc.* 2023; *in press*. [CrossRef]
22. Zhang, S.; Zhou, J.; Fu, F.; Hu, G.; Zhao, Y.; Wang, L.; Xu, Y. Electric arc electrochemical machining of Ti6Al4V titanium alloy based on high-pressure internal flushing fluid. *J. Manuf. Process.* **2024**, *112*, 60–81. [CrossRef]

23. Yang, P.J.; Hung, J.C. On high resolution bubbly flow generator for gas-mixed micro electrochemical machining. *J. Manuf. Process.* **2024**, *121*, 269–288. [CrossRef]
24. Jeong, J.; Kurniawan, R.; Kwak, Y.I.; Yoon, I.C.; Ali, S.; Ko, T.J. Helical groove texturing on flutes of twist drill and hole machining enhancement. *J. Manuf. Process.* **2024**, *129*, 307–318. [CrossRef]
25. Du, C.; Dai, Y.; Hu, H.; Guan, C.L.; Liu, J.F.; Lai, T.; Tian, Y.Y. Atomic-level insight into process and mechanism of ion beam machining on aluminum optical surface. *Vac. Technol. Appl. Ion Phys. Int. J. Abstr. Serv. Vac. Sci. Technol.* **2024**, *222*, 113011. [CrossRef]
26. Xie, L.; Tian, Y.; Shi, F.; Guo, S.P.; Zhou, G. Adaptive processing strategy of pulse ion beam for sub-nanometer precision optical components. *J. Mater. Process. Technol.* **2024**, *327*, 119341. [CrossRef]
27. Wang, X.; Peng, Y. Electrochemical micromachining on nickel and nickel-based superalloys with two-tone sinusoidal signal. *Electrochem. Commun.* **2024**, *158*, 107642. [CrossRef]
28. Liu, S.; Li, C.; Jin, X.; Ma, D.F.; Yan, Q.; Liu, G.D.; Cao, X.; Wang, H. Solid dielectric electrochemical polishing of 3D-printed parts Performance and mechanisms. *Int. J. Mech. Sci.* **2025**, *285*, 109822. [CrossRef]
29. Chen, D.; Liu, Z.; Li, L.; Wang, W.A.; Zhou, J.X.; Song, J.L. Manufacturing of dies and an experimental study on the cold-press surface-texture forming process. *J. Manuf. Process.* **2023**, *99*, 27–37. [CrossRef]
30. Ge, Z.; Wu, H.; Hu, Q.; Zhu, H.T.; Zhu, Y.W. Uniformity enhancement of flow field through optimizing nozzle structure for jet electrochemical machining. *Int. J. Electrochem. Sci.* **2024**, *19*, 100809. [CrossRef]
31. Zhai, K.; Liang, Y.; Li, T.; Ma, S.H.; Du, L.Q. Research on jet electrochemical machining with coaxial megasonic assistance. *Ultrason. Sonochem.* **2024**, *110*, 107054. [CrossRef] [PubMed]
32. Liu, Y.; Qu, N.; Li, H.; Zhang, Z.Y. Boundary fluid constraints during electrochemical jet machining of large size emerging titanium alloy aerospace parts in gas–liquid flows Experimental and numerical simulation. *Chin. J. Aeronaut.* **2025**, *38*, 103024. [CrossRef]
33. Zhao, Y.; Lyu, Z.; Liu, W.; Zhang, B.; Clare, A.T. Submerged electrochemical jet machining with in-situ gas assistance. *CIRP Ann.* **2024**, *73*, 117–120. [CrossRef]
34. Liu, W.; Cheng, A.; Dong, H.; Zhao, Y.H. Electrochemical jet machining in deep-small holes with gas assistance: Generating complex features on internal surfaces. *J. Mater. Process. Technol.* **2025**, *335*, 118662. [CrossRef]
35. Yu, M.; Du, L.; Zhai, K.; Chen, H.H.; Wang, F.L.; Li, A.Q.; Wang, Z.M. Towards understanding uniformity of megasonic-assisted through-mask electrochemical micromachining based on bubble dynamics. *J. Manuf. Process.* **2023**, *96*, 125–137. [CrossRef]
36. Liu, Z.; Lian, Z.; Yang, J.; Xu, J.K.; Tian, Y.L.; Yu, H.D. High-efficient and scalable fabrication of robust superhydrophobic microarrays through maskless electrochemical machining. *Colloids Surf. A Physicochem. Eng. Asp.* **2024**, *681*, 132700. [CrossRef]
37. Jakob, L.; Bartsch, J. Influences on the anisotropy in through-mask electrochemical micromachining processes. *Electrochim. Acta* **2025**, *511*, 145366. [CrossRef]
38. Yang, X.; Du, L.; Li, A.; Wu, M.X.; Wu, C.H.; Li, J.M. A novel method of induction electrode through-mask electrochemical micromachining. *Int. J. Mach. Tools Manuf.* **2024**, *203*, 104221. [CrossRef]
39. Guerrero-Vacas, G.; Fusco, S.; Rodríguez-Valverde, M.Á.; Alabanda, O.R. Manufacturing hydrophobic surfaces on aluminium substrates by micro-milling with end-ball nose tools. *J. Manuf. Process.* **2024**, *124*, 24–37. [CrossRef]
40. Li, Z.; Zhou, W.; Liu, G.; Luo, H.P.; Zhang, Y.J. Study on micro electrochemical milling with programmable dynamic eccentric rotating electrode. *Precis. Eng.* **2024**, *91*, 300–320. [CrossRef]
41. Wang, S.; Liu, J.; Bao, C.; Zhu, D. Flow field design and experiment of high-efficiency electrochemical milling with large machining area. *Chin. J. Aeronaut.* **2025**, *38*, 103211. [CrossRef]
42. Shen, Z.; Li, H.; Zhang, J.; Qu, N. Improving flatness of machined surface in rotating cathode electrochemical milling. *J. Manuf. Process.* **2024**, *116*, 60–76. [CrossRef]
43. Cui, G.; Wang, D.; Zhu, Z.; Zhou, S.F. Accuracy analysis and improvement methods for revolving parts in counter-rotating electrochemical machining with continuous radial feeding. *CIRP J. Manuf. Sci. Technol.* **2024**, *54*, 43–56. [CrossRef]
44. Yu, T.; Wang, S.; Liu, X.; Liu, S.J.; Shi, C.; Du, N. Electrochemical corrosion behavior of 7075 aluminum alloy with different ultrasonic surface rolling microstructures. *J. Mater. Res. Technol.* **2024**, *30*, 4702–4713. [CrossRef]
45. Zhou, S.; Wang, D.; Cui, G.; Zhang, J.; Zhu, D. Co-rotating electrochemical machining of convex structures on the inner surface of annular parts using a flexible cathode tool. *Precis. Eng.* **2024**, *89*, 55–69. [CrossRef]
46. Yang, J.; Wang, Y.; Yang, Y.; Liu, Y.F.; Zhang, W.W. Fabrication of micro holes with confined pitting corrosion by laser and electrochemical machining: Pitting corrosion formation mechanisms and protection method. *J. Mater. Process. Technol.* **2025**, *335*, 118677. [CrossRef]
47. Geng, T.; Xu, Z.; Lu, J. A sustainable, high-quality method for machining film cooling holes: Cryogenic airflow-assisted electrochemical discharge drilling. *J. Clean. Prod.* **2023**, *426*, 139017. [CrossRef]
48. Wang, M.; Zhang, R.; Shang, Y.; Zheng, J.S.; Wang, X.D.; Xu, X.F. Micro-milling microstructures in air-shielding ultrasonic assisted electrochemical machining. *J. Manuf. Process.* **2023**, *97*, 171–184. [CrossRef]

49. Wang, C.Y.; Li, Z.; Xu, P.; Hou, Y.Q.; Tan, D.P.; Li, L. Collision modelling approach and transient response mechanism of ring-ribbed cylindric shells for underwater vehicles. *Appl. Math. Model.* **2025**, *141*, 115923. [CrossRef]
50. Pandey, H.; Pawar, K.; Dixit, P. Fabrication of through alumina vias (TAV) by ultrasonic micromachining for advanced packaging applications. *Mater. Sci. Semicond. Process.* **2025**, *185*, 108923. [CrossRef]
51. Zheng, G.A.; Weng, X.X.; Wang, T.; Xu, P.; Xu, W.X.; Li, L.; Xu, X.F.; Tan, D.P. Piezoelectric ultrasonic coupling-based polishing of micro-tapered holes with abrasive flow. *J. Zhejiang Univ.-Sci. A*, 2025; *in press*.
52. Ren, M.; Zhu, D.; Zhou, X.; Wang, Y.M.; Li, S.L. Surface quality enhancement in ultrasonic vibration-assisted electrochemical machining. *Colloids Surf. A Physicochem. Eng. Asp.* **2024**, *703*, 135188. [CrossRef]
53. Zhang, Y.; Ni, Q.; Ouyang, Z.; Bian, H.W.; Bu, T.Q. Controllable vertical and radial corrosion by step flow fields for fabricating large aspect ratio micro-cone arrays in through-mask electrochemical micromachining. *J. Mater. Process. Technol.* **2025**, *335*, 118664. [CrossRef]
54. Chen, Z.; Liu, Y.; Wang, T.; Wang, K. Ultrasonic assisted electrochemical discharge milling of complex glass microstructure with high-quality. *J. Manuf. Process.* **2023**, *94*, 94–106. [CrossRef]
55. Wang, P.; Hu, J.; Hu, H.; Yu, D.G.; Yin, Z.; Zou, H.Y.; Lai, T. Debris motion and taper suppression in EDM deep hole machining assisted by longitudinal/torsional ultrasonic vibration. *J. Manuf. Process.* **2025**, *133*, 798–810. [CrossRef]
56. Huang, Y.; Fang, C.; Yang, F.; Gong, S.L.; Wang, X. Experimental investigation of electrochemical machining for involute internal spline using cathode working teeth sheet with circumferential vibration. *Precis. Eng.* **2024**, *88*, 905–914. [CrossRef]
57. Xu, X.; Ma, Y.; Gong, Y.; Li, H.; Wang, Z.C.; Niu, P.F.; Pang, W. Mass-loaded suspended piezoelectric micromachined ultrasonic transducer array towards flexible stretchable electronics evaluation. *Sens. Actuators A. Phys.* **2025**, *381*, 116048. [CrossRef]
58. Tan, Y.F.; Ni, Y.S.; Xu, W.X.; Xie, X.S.; Li, L.; Tan, D.P. Key technologies and development trends of the soft abrasive flow finishing method. *J. Zhejiang Univ.-Sci. A Appl. Phys. Eng.* **2023**, *24*, 1043–1064. [CrossRef]

Disclaimer/Publisher's Note: The statements, opinions and data contained in all publications are solely those of the individual author(s) and contributor(s) and not of MDPI and/or the editor(s). MDPI and/or the editor(s) disclaim responsibility for any injury to people or property resulting from any ideas, methods, instructions or products referred to in the content.